




Article

Surface Morphological Features of Molybdenum Irradiated by a Single Laser Pulse

Roberto Montanari ^{*}, Ekaterina Pakhomova, Riccardo Rossi , Maria Richetta 
and Alessandra Varone

Department of Industrial Engineering, University of Rome “Tor Vergata”, 00133 Rome, Italy; pakhomovaea@mail.ru (E.P.); r.rossi@ing.uniroma2.it (R.R.); richetta@uniroma2.it (M.R.); alessandra.varone@uniroma2.it (A.V.)

* Correspondence: roberto.montanari@uniroma2.it; Tel.: +39-6-7259-7182

Received: 19 December 2019; Accepted: 9 January 2020; Published: 11 January 2020



Abstract: Molybdenum (Mo) is considered a plasma facing material alternative to tungsten (W) for manufacturing the divertor armours of International Thermonuclear Experimental Reactor (ITER). Transient thermal loads of high energy occurring in a tokamak during the service life have been simulated through a single laser pulse delivered by a Nd:YAG/Glass laser, and the effects have then been examined through scanning electron microscopy (SEM) observations. An erosion crater forms in correspondence with the laser spot due to the vaporization and melting of the metal, while all around a network of cracks induced by thermal stresses is observed. The findings have been compared to results of similar experiments on W and literature data. The morphology of the crater and the surrounding area is different from that of W: the crater is larger and shallower in the case of Mo, while its walls are characterized by long filaments, not observed in W, because the lower viscosity and surface tension of Mo allow an easier flow of the liquid metal. Most importantly, the volume of Mo ablated from the surface by the single laser pulse is about ten times that of W. This critical aspect is of particular relevance and leads us to conclude that W remains the best solution for manufacturing the armours of the ITER divertor.

Keywords: molybdenum; nuclear fusion reactors; laser; surface damage; microstructure

1. Introduction

Plasma facing materials (PFM) of future nuclear fusion reactors will be exposed, in addition to a steady state heat flux, to transient events of high energy such as disruption, edge localized modes (ELM), and vertical displacement events (VDE). The large heat fluxes occurring during transient events induced by plasma instabilities may lead to the melting and vaporization of PFMs with the consequent contamination of plasma and the damage of PFM components.

At present, tungsten (W) and W-1%La₂O₃ alloy are the most promising materials for manufacturing the divertor armours of ITER [1–5]. W has the highest melting point of all metals and exhibits excellent thermo-mechanical characteristics, a low sputtering rate, and a tritium inventory; therefore, thin W coatings on graphite and carbon fibre composites have already been adopted in reactors like JET [5] and ASDEX-U [6]. The drawbacks of W are the poor machinability at an ambient temperature and the high ductile-to-brittle transition temperature. Moreover, the resistance to thermal shocks during ELMs is also a matter of concern [7] because a fibrous nanostructure forms on the W surface due to low-energy He ion irradiation with detrimental effects on the thermo-mechanical properties [8].

The dispersion of La₂O₃ particles in the W matrix improves the toughness [9], enhances the resistance to thermal shocks and creep, increases the recrystallization temperature, and hinders grain growth at a high temperature (up to ~1750 °C).

Some studies were also carried out to assess the effects of the dispersion in W of other oxides (Y_2O_3 , TiO, etc.) or other elements (Ta, Ti), with controversial results [10,11]. In fact, some properties resulted in being improved; however, the added components often involve the generation of W dust into plasma; thus, as of now, all the required conditions to develop a reliable divertor armour have not been satisfied.

Recently, molybdenum (Mo) has attracted increasing interest as a possible PFM alternative to W [12–16]. As shown in Table 1, Mo is a high-Z refractory metal with very good physical properties (density, melting point, boiling point, and thermal conductivity), even if it is a little inferior to W. On the contrary, the ductile to brittle transition temperature (DBTT) of Mo is much lower, and it exhibits a better resistance to thermal shocks [15–17].

Table 1. A comparison of some physical properties of W and Mo: atomic number Z , density ρ_A , melting point T_M , boiling point T_B , thermal conductivity ξ , ductile to brittle transition temperature DBTT, latent heat of fusion E_M , and latent heat of vaporization E_V .

Metal	Z	ρ_A at 20 °C [g·cm ⁻³]	T_M [°C]	T_B [°C]	ξ [W·m ⁻¹ ·K ⁻¹]	DBTT [°C]	E_M [kJ·mole ⁻¹]	E_V [kJ·mole ⁻¹]
W	74	19.25	3422	5555	110	+400	35.4	824
Mo	42	10.22	2623	4639	142	-20	32	598

Another relevant advantage of Mo to W is its behavior under prolonged irradiation by 14 MeV neutrons of a fusion power plant. W transmutes to osmium (Os) via rhenium (Re) and forms the W–Os–Re alloy. Cottrell [18] calculated that five years in a fusion power plant will have transmuted pure W into an alloy of about 75 (at.%) W, 13 (at.%) Os, and 12 (at.%) Re, a composition close to that of the brittle σ phase. In the same irradiation conditions, Mo would produce 1.1% Tc and 0.65% Ru after 5 years, well inside the primary Mo phase field at 1500 °C.

The erosion/redeposition characteristics of pure Mo and W are similar [19], but the fractional hydrogen isotope retention is lower in Mo than in W [20].

In this work the specific conditions of transient events have been simulated by irradiating Mo samples through a Nd:YAG/Glass high power laser source, suitable to release a high thermal load in a very short time (~15 ns) on a small area (~200 μ m) and to reach a surface power density on the focal plane of about 1.7×10^{12} W·cm⁻².

The effects of the laser pulse on the sample surface have been then investigated through 3D surface analysis and scanning electron microscopy (SEM) observations. The same experimental procedure was adopted in previous works of present authors to study the behavior of W (bulk and plasma sprayed) [21,22] and W-1%La₂O₃ alloy [23]. The results are discussed in comparison to those previously obtained by us on W, the principal candidate material for building the armours of ITER, and in general to literature data. A recent critical overview about material erosion of candidate materials like W and Mo is reported in [24].

2. Material and Experimental Section

2.1. Sample Characteristics

The material (purity of 99.9 wt.%) examined in the present work was supplied by PLANSEE (Metallwerk Plansee, Reutte, Austria) in the form of plates with a thickness of 25 mm, which were cut to obtain samples with dimensions of 25 mm \times 20 mm (Figure 1a).

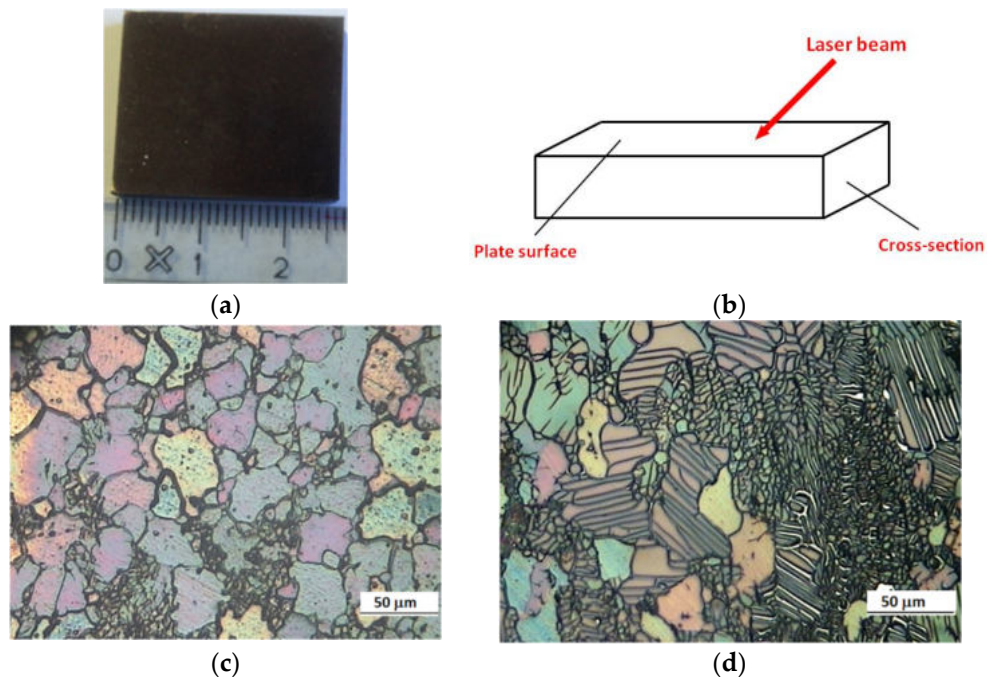


Figure 1. Picture(a) and (b) sketch of the sample. The structure of the examined Mo samples: plate surface (c), cross-section (d).

The structure of Mo grains on the plate surface and in the cross-section (Figure 1b) has been examined through light microscopy. After conventional metallographic surface preparation, the sample has been etched by immersion for 60 s in a boiling solution of H₂O 100 mL with H₂O₂ (30%) 1 mL, and observed by using an optical microscope (Union Optical Co., Ltd., Tokyo, Japan).

Figure 1c,d shows how the grain structure is different on the plate surface (c) and in the cross-section (d). A large part of the plate surface is covered by grains with a mean size D of about 40 μm , while some zones exhibit smaller grains of about 5 μm (Figure 1b). In the cross-section, small grains ($\sim 5 \mu\text{m}$) are the dominant feature, and only few grains of larger size are present and show elongated substructures.

The Mo samples were then characterized through X-ray diffraction (XRD, diffractometer Philips, Eindhoven, The Netherlands). Figure 2 displays the XRD pattern obtained by focusing the beam on the plate surface.

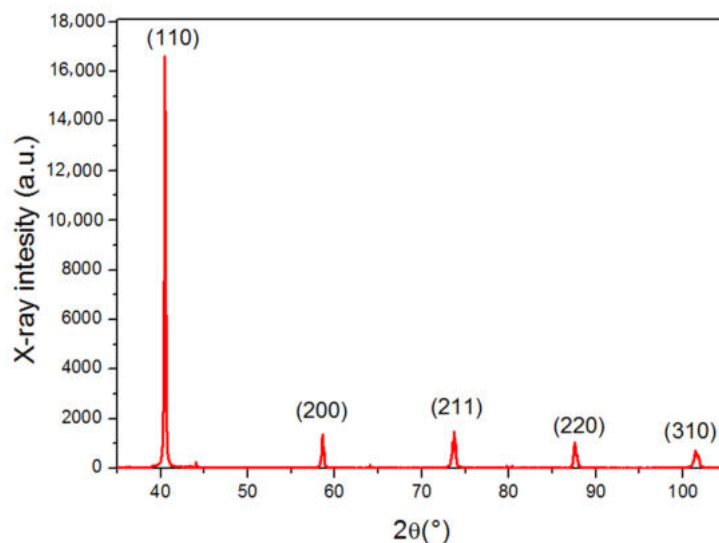


Figure 2. The XRD pattern of the examined Mo.

The XRD pattern displayed in Figure 2 was collected by operating in a step-scanning mode with Cu-K α radiation (wavelength $\lambda = 0.1508$ nm), 2θ steps of 0.05° , and a counting time of 5 s per step. To assess the possible presence of preferred grain orientations, the relative intensities of the main reflections have been compared to those reported in the JCPDS-ICDD database [25], file 42-1120, and corresponding to a material with random oriented grains. The results displayed in Table 2 show that Mo used in the present experiments exhibits a strong {110} texture.

Table 2. A comparison of the intensities of main reflections to those reported in the JCPDS-ICDD database.

Miller Index $\{hkl\}$	110	200	211	220	310
JCPDS-ICDD	100	16	31	9	14
Sample	100	8	9	6	4

To determine the cell parameter and the dislocation density, high precision peak profiles were recorded with 2θ steps of 0.005° and a counting time of 5 s per step. The cell parameter a resulted in 0.3150 nm, very close to the value of 0.3147 nm given by the JCPDS-ICDD database.

The dislocation density ρ has been determined from the line broadening of XRD peak profiles. The total line broadening β_T of a peak is the sum of two contributions due to the size D of coherently diffracting domains (β_D), namely the grains, and to the micro-strains ε (β_ε):

$$\beta_T = \beta_D + \beta_\varepsilon = \frac{K\lambda}{D \cos \theta} + 2\varepsilon \tan \theta \quad (1)$$

θ being the Bragg angle and $K = 0.89$. Since the mean D value is ~ 10 μm , β_D is negligible and $\beta_T \cong \beta_\varepsilon$. The dislocation density ρ has then been calculated using the Williamson-Smallman relationship [26]:

$$\rho = \Xi \varepsilon^2 / k_0 b^2 \quad (2)$$

where $\Xi = 16.1$ and $k_0 \cong 1$ are constants, and $b = 0.18186$ nm is the modulus of Burgers vector. The dislocation density ρ resulted in 2.0×10^{10} cm^{-2} .

The samples were also submitted to Vickers micro-hardness tests (Shimadzu corporation, Kyoto, Japan). The mean value obtained from 20 tests (300 g, 10 s) was 211 ± 5 HV. The yield stress $\sigma_Y = 540$ MPa was determined from the FIMEC test [27].

2.2. Laser Source

The plate surface of the Mo samples have been irradiated (see Figure 1) by a single laser pulse delivered by the laser system—Tor Vergata Laser-Plasma Source (TVLPS) [28], a no-commercial device which consists of a Nd:YAG oscillator, based on the Q-switched technique, followed by four amplification stages. The first two are also Nd:YAG, while the last ones are Nd:Glass. The pulse parameters of the present experiments are: wavelength $\lambda = 1064$ nm, pulse duration $\Delta\tau \approx 15$ ns, pulse energy $E_p \approx 8$ J, Transverse Electromagnetical Mode is TEM00, P-polarized, focal spot size $\Phi = 200$ μm , and surface power density on the focal plane $I = 1.7 \times 10^{12}$ $\text{W}\cdot\text{cm}^{-2}$. The plasma electronic temperature at the critical surface ($T_e \approx 1.218 \times 10^6$ K) simulates the conditions of transient events occurring in a tokamak due to plasma instability.

The experiments were carried out in a vacuum chamber ($P \approx 10^{-5}$ bar), and the laser beam hits the samples with an incidence angle of 45° to minimize debris projection near the target. More details about the experimental set-up are reported in previous works [21–23] on W (bulk and plasma sprayed) and W-1%La₂O₃ alloy, which were irradiated in the same conditions.

A spectrometer USB 2000 model (Ocean Optics, 4301 Metric Drive, Winter Park, FL, USA) was used to collect the spectrum from plasma induced by a laser pulse.

After laser irradiation, the surface morphological changes of the Mo samples were studied through SEM observations (Hitachi SU70, Hitachi, Tokyo, Japan). A 3D surface analyzer (TalySurf CLI 2000, Taylor Hobson, Leicester, UK) was used to get level profiles in the zone hit by the laser spot.

3. Results and Discussion

Figure 3 displays the spectrum recorded from plasma induced by a laser pulse through the spectrometer USB 2000. It only exhibits the lines of Mo, whereas those of other metals are not present. Some lines of low intensity corresponding to O are also detected and can be attributed to native oxide on the sample surface.

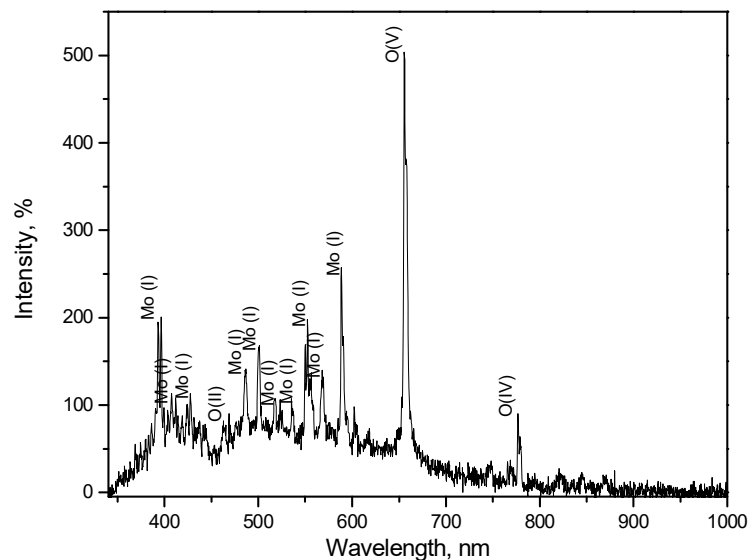


Figure 3. Spectrum recorded from plasma induced by a laser pulse (wavelengths from 250 to 1000 nm).

The zone on the sample surface affected by laser pulse irradiation is almost circular with a diameter of ~ 2.2 mm (Figure 4), i.e., much larger than that of the laser spot ($\Phi = 200$ μm).

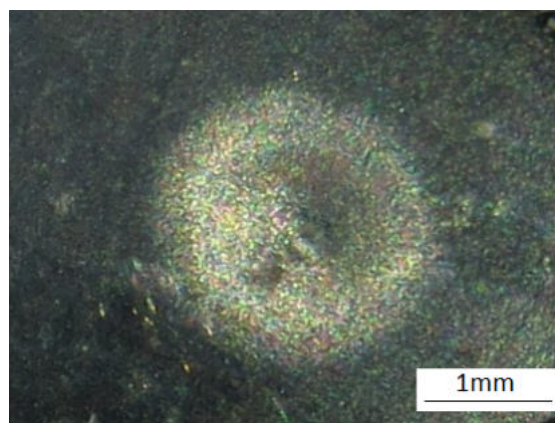


Figure 4. The surface zone affected by the laser pulse.

As shown in the SEM micrographs of Figure 5, an erosion crater with a diameter of ~ 300 μm (a) forms in the central area of the laser spot where the beam has the highest intensity. The laser intensity has a Gaussian shape; thus, its maximum is at the centre, and it radially decreases toward the periphery. The larger fraction of the energy is released in the central part of the spot, causing the melting and vaporization of the metal; the crater formation is due to the ejection of part of the molten metal. Figure 5b displays a drop of the ejected metal fallen and re-solidified in a zone near the

crater. Sinclair et al. [16] demonstrated that the surface melting of Mo begins when the energy density reaches a value of $\sim 1.0 \text{ MJ}\cdot\text{m}^{-2}$ and that the droplet formation and boiling starts from $\sim 1.4 \text{ MJ}\cdot\text{m}^{-2}$, namely values much lower than those involved in the present experiments.

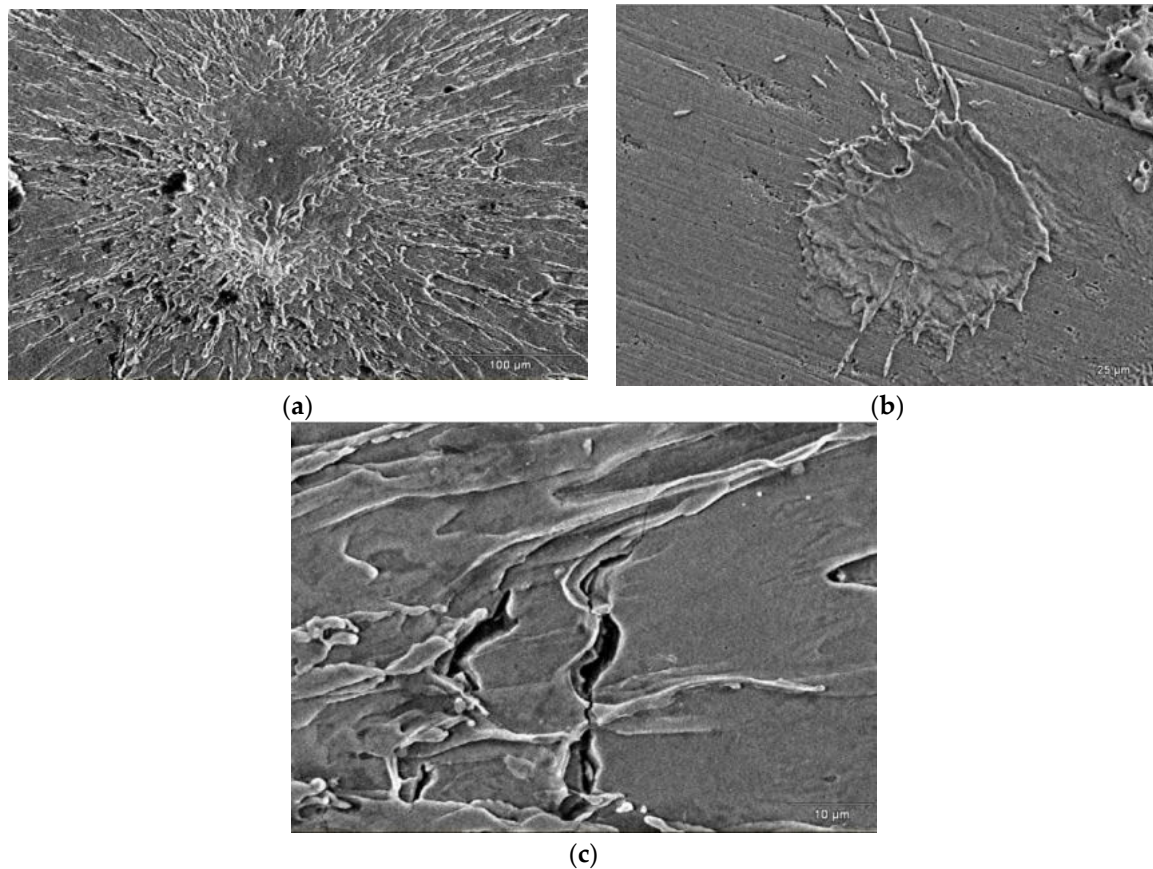


Figure 5. SEM micrographs displaying the zone irradiated by the laser pulse: (a) the crater; (b) the splash of molten metal ejected from the crater; and (c) a detail of the crater at a higher magnification showing some cracks.

Another effect resulting from the Gaussian intensity profile of the spot is the occurrence of a temperature gradient in molten metal leading to a liquid movement along the radial direction, giving rise to the typical morphology of crater walls shown in the detail of Figure 5c and to the formation of a ridge around the crater. The crater walls are decorated by radially oriented filaments that are produced by the movement and successive solidification of the liquid metal.

The thermal stresses arising from the rapid heating and successive cooling of the external zone of the crater lead to the nucleation and growth of cracks like those shown in Figure 5c.

The morphology of the area affected by the laser pulse has been recorded through a 3D surface analyzer (see Figure 6a), and 10 level profiles of the crater, such as that displayed in Figure 6b, have been measured along different directions. The mean diameter and depth was 300 ± 9 and $17 \pm 2 \mu\text{m}$, respectively; thus, the aspect ratio of the crater (depth/diameter) is ~ 0.05666 . The shape of the crater is quite different from that produced in W under the same experimental conditions (crater diameter = $75 \mu\text{m}$, depth = $25 \mu\text{m}$, and aspect ratio ~ 0.333 [21]), namely in the case of Mo it is larger and shallower. Such difference can be explained by considering the specific microstructure of the examined Mo and W samples and its relation with the thermal conductivity affecting the heat flow through the materials. Since the correlation between incoming and outgoing phonons is destroyed

by the scattering occurring at an interface like a grain boundary [29,30], the thermal conductivity C decreases with the decreasing grain size d and can be written as:

$$C = \frac{C_0}{1 + \frac{R_K C_0}{d}} \quad (3)$$

where C_0 is the grain interior thermal conductivity and R_K is the Kapitza resistance that measures the interface resistance to the thermal flow [31,32].

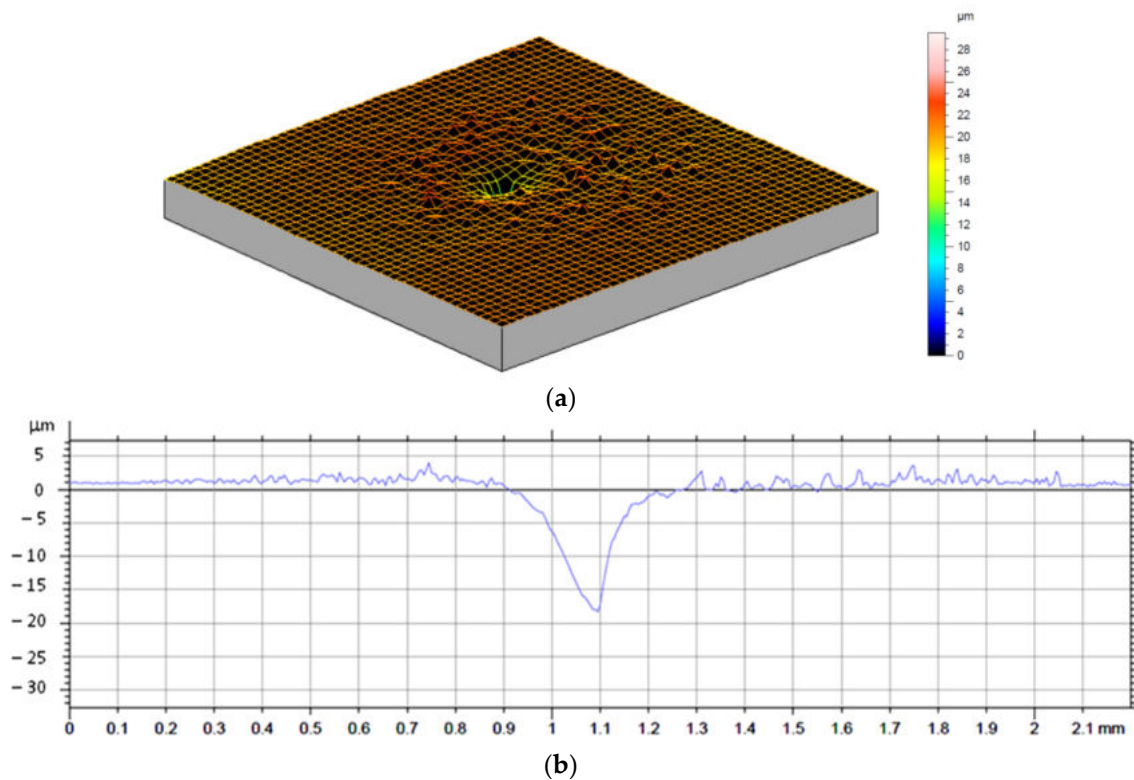


Figure 6. (a) The morphology of the laser irradiated zone measured through a 3D surface analyzer. A level profile of the crater determined from the image in (a) is displayed in (b).

W has equiaxed grains; thus, there is not a preferred direction for the heat flow, as a result of which the crater diameter and depth are comparable. On the contrary, in the case of Mo, heat moves easier along the surface than in the perpendicular direction because it encounters a lower number of interfaces (see Figure 1b,c), giving rise to a larger and shallower crater.

However, the most important difference between the behaviour of the two refractory metals regards the volume of material ablated from the surface by the single laser pulse. A rough estimation of such a volume has been made by considering the crater like a cone. From this calculation, the ablated volume in the case of Mo is about ten times that of W. This strictly depends on the latent heat of fusion E_M and latent heat of vaporization E_V of W, which are remarkably higher than those of Mo (see Table 1).

After melting, the liquid metal is flushed to the periphery, and its viscosity and surface tension determine the morphological features of the crater and surrounding zones, which are different from those of W because in that case [21,22] solidified drops decorating the crater walls have been observed but the long filaments displayed by Mo have not (see Figure 5).

The surface tension of Mo, determined by Paradis et al. [33] through the oscillation drop technique in conjunction with a vacuum electrostatic levitation furnace, can be expressed as:

$$\sigma(T) = 2.29 \times 10^3 - 0.26(T - T_m) \text{ (mN}\cdot\text{m}^{-1}) \quad (4)$$

while that of W is [34]:

$$\sigma(T) = 2.48 \times 10^3 - 0.31(T - T_m) \text{ (mN}\cdot\text{m}^{-1}) \tag{5}$$

The surface tension values of molten Mo and W vs. temperature, calculated according to Equations (4) and (5), are plotted in Figure 7.

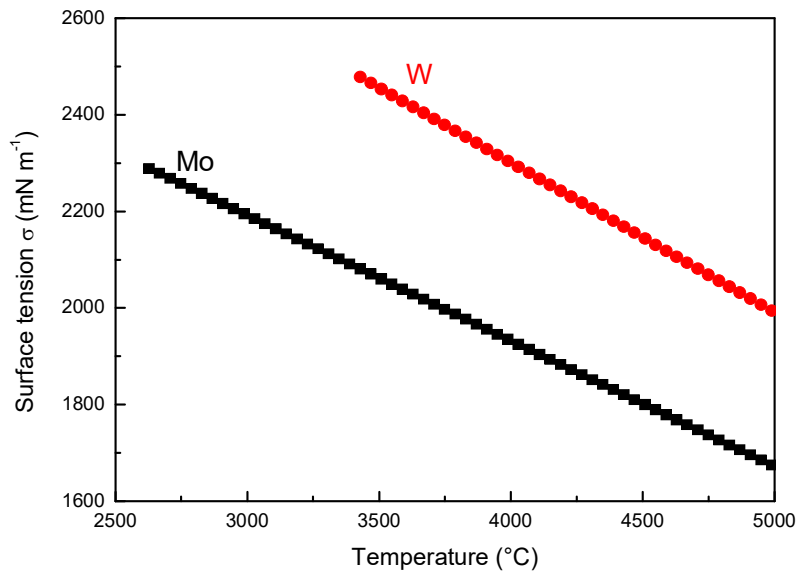


Figure 7. Surface tension of W and Mo vs. temperature, calculated according to the relationships of Paradis et al. [33,34].

The viscosity trends of liquid Mo [33–35] and W [36] vs. temperature are given by the Equations (6) and (7), respectively, and are plotted in Figure 8.

$$\eta(T) = 0.27\exp[73 \times 10^3/RT] \text{ (mPa}\cdot\text{s)} \tag{6}$$

$$\eta(T) = 0.16\exp[3.9713T_M/T] \text{ (mPa}\cdot\text{s)} \tag{7}$$

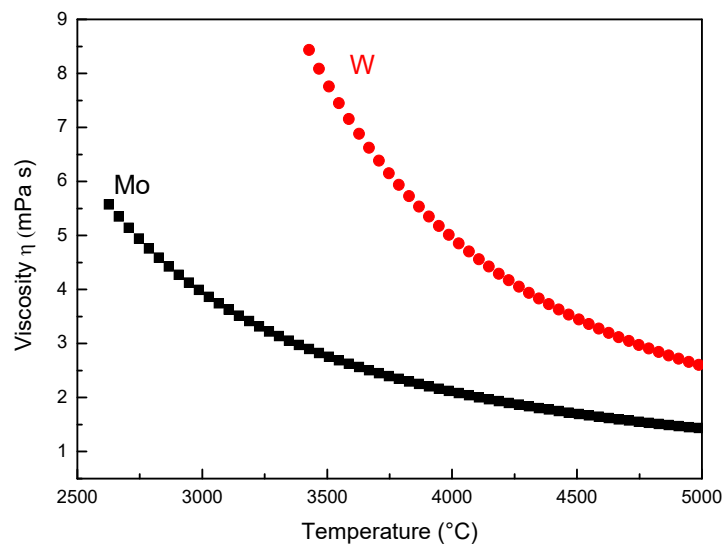


Figure 8. Viscosity of W and Mo vs. temperature, calculated according to Equations (5) and (6).

On these grounds, it is clear that the lower viscosity of Mo allows an easier flow of the liquid metal, leading to the formation of long filaments (see Figure 5) that are not observed in the case of W.

In a more external region outside the crater, from 300 μm to ~ 1 mm, the material exhibits bubbles like those shown in Figure 9a,b and long cracks. Such cracks are due to thermal stresses occurring in the metal after fast heating and successive cooling; as shown in Figure 9c, they depart from the bubbles to then propagate through the material. Similar results have been recently published by Straus et al. [37], who studied the damage of W and Mo surfaces induced by an ultraviolet laser radiation ($\lambda \sim 47$ nm).

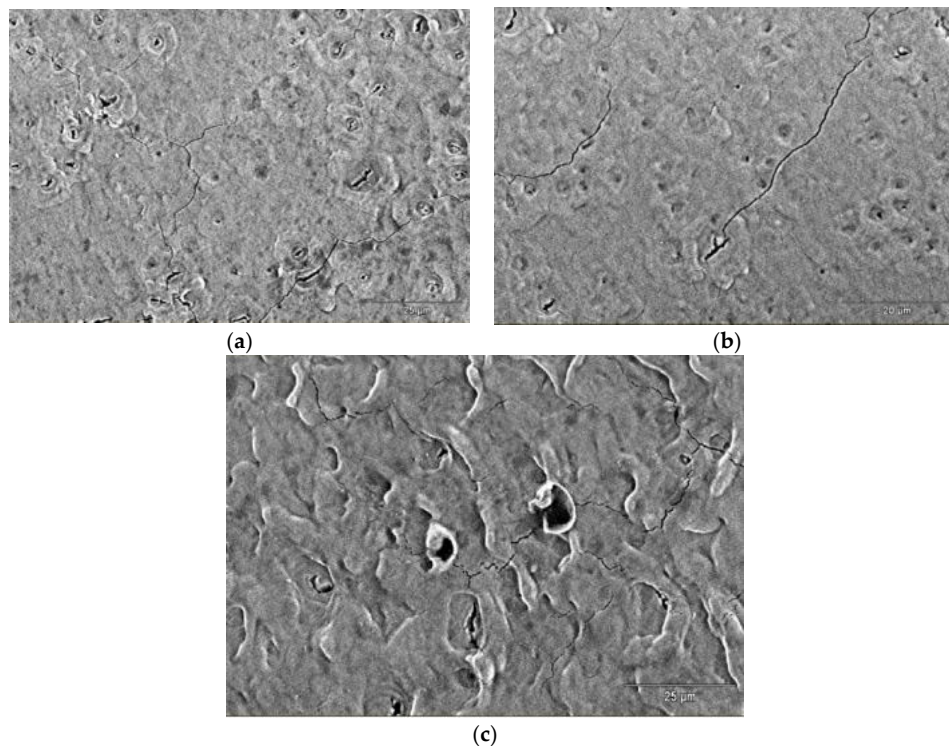


Figure 9. (a–c) The zone around the crater exhibits bubbles and long cracks often departing from the bubbles.

Figure 10a shows a cross-section of the crater: the morphology and size of the grains differs remarkably from that of the unaffected material (Figure 1c), since elongated substructures substantially disappeared, and grains with a size of a few microns cover only a small part of the observed area. The change can be explained by the grain growth induced by the strong heating in the zone close to where the melting occurs. The same phenomenon is also observed in Figure 10b, taken from a zone below the crater at a distance of about 500 μm from the sample surface, even if in this case the effect is limited because the larger distance involves a lower temperature increase.

Finally, no microstructural change has been detected at a distance of about 1 mm.

In future work, research will be focused on the regimes of high-energy exposure in order to explore the effects of different thermal loads. Treatments suitable for improving the structure and mechanical properties of Mo will also be investigated in order to get better behaviour under laser irradiation and to eliminate surface cracking. Another aspect that deserves to be deeply examined is the role of the original sample roughness, which can affect the erosion as well as tritium retention (e.g., see the paper of Eksaeva et al. [38]). However, the most critical aspect evidenced by the present experiments, namely the large volume ablated from the surface by the single laser pulse (\sim ten times that of W), seems difficult to resolve because the latent heat of fusion and latent heat of vaporization are intrinsic properties of the material and are not easily modifiable. On these grounds, W remains the first choice for manufacturing the armours of the ITER divertor, even if the decrease of DBTT and the increase

of ductility and fracture toughness are mandatory requirements for a successful application of the material. Aiming for this goal, three approaches are currently being studied to ductilize W [17,39,40]: (i) the preparation of W solid solutions (Re, Ir, Ta, and V are the most promising alloying elements), (ii) the synthesis of ultra-fine-grained W, and (iii) the synthesis of W composites. The last one consists in reinforcing a W matrix through W fibres coated by an engineered interface and seems to guarantee the best results.

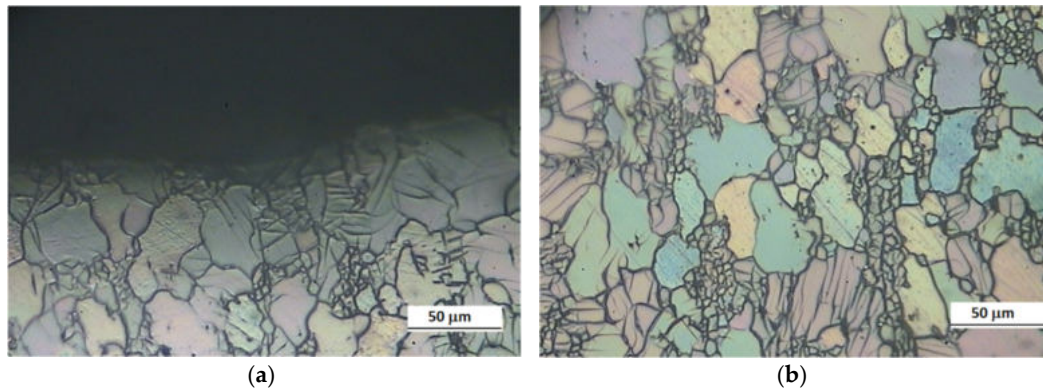


Figure 10. (a) Cross-section of the crater and (b) of the zone just below.

4. Conclusions

The effects on Mo of transient high energy thermal loads occurring in a Tokamak during operative conditions have been simulated through a single laser pulse delivered by a Nd:YAG/Glass laser.

The examination of the irradiated zone evidenced that an erosion crater forms in the spot's central area due to metal vaporization and the ejection of molten metal. The thermal gradient leads to radial flushing of liquid metal, giving rise to a ridge around the crater and long filaments along the crater walls. Moreover, in a more external area (up to a distance of about 1 mm from the laser spot center), the surface shows bubbles and long cracks.

The results have been compared to those of previous experiments carried out in the same conditions on W, the material considered to be the principal candidate for building the armours of ITER.

Although some morphological features, namely the presence of an erosion crater at the centre of a more extended zone with surface modifications, are similar in Mo and W, these metals exhibit relevant differences:

- the crater is larger and shallower in the case of Mo;
- the volume of Mo ablated from the surface by a single laser pulse is about ten times that of W owing to the remarkably higher latent heat of fusion and latent heat of vaporization of W;
- the morphological features of the Mo crater walls are characterized by long filaments, not observed in the case of W, because the lower viscosity and surface tension of Mo allow an easier flow of the liquid metal;
- grain growth has been observed in a material layer of about 1 mm under the crater, with the effects decreasing as the distance from the surface increases.

In conclusion, the higher erosion of Mo indicates that W remains the best solution for manufacturing the armours of the ITER divertor.

Author Contributions: Conceptualization, R.M., E.P., R.R., M.R. and A.V.; Data curation, R.M., E.P., R.R., M.R. and A.V.; Investigation, E.P., R.R., M.R. and A.V.; Supervision, R.M.; Writing—original draft, R.M., E.P. and M.R. All authors have read and agreed to the published version of the manuscript.

Funding: This work has been carried out within the framework of the EUROfusion Consortium and has received funding from the Euratom research and training programme 2014–2018 and 2019–2020 under Grant Agreement No. 633053. The views and opinions expressed herein do not necessarily reflect those of the European Commission.

Acknowledgments: The authors are grateful to Piero Plini and Benedetto Iacovone of Department of Industrial Engineering for the assistance in sample preparation.

Conflicts of Interest: The authors declare no conflict of interest.

References

1. Riccardi, B.; Pizzuto, A.; Orsini, A.; Libera, S.; Visca, E.; Bertamini, L.; Casadei, F.; Severini, E.; Montanari, R.; Vesprini, R.; et al. Tungsten thick coatings for plasma facing components. *Fusion Technol.* **1998**, *31*, 223–226.
2. Roedig, M.; Kuehnlein, W.; Linke, J.; Merola, M.; Rigal, E.; Schedler, B.; Visca, E. Investigation of tungsten alloys as plasma facing materials for the ITER divertor. *Fusion Eng. Des.* **2002**, *61*, 135–140. [[CrossRef](#)]
3. Bolt, H.; Barabash, V.; Krauss, W.; Linke, J.; Neu, R.; Suzuki, S.; Nyoshida, N. Materials for the plasma facing components of fusion reactors. *J. Nucl. Mater.* **2004**, *329*, 66–73. [[CrossRef](#)]
4. Uytendhouwen, I.; Decreton, M.; Hirai, T.; Linke, J.; Pintsuk, G.; Van Oost, G. Influence of recrystallization on thermal shock resistance of various tungsten grades. *J. Nucl. Mater.* **2007**, *363*, 1099–1103. [[CrossRef](#)]
5. Maier, H.; Hirai, T.; Rubel, M.; Neu, R.; Mertens, P.; Greuner, H.; Hopf, C.; Matthews, G.F.; Neubauer, O.; Piazza, G.; et al. Tungsten and beryllium armour development for the JET ITER-like wall project. *Nucl. Fusion* **2007**, *47*, 222. [[CrossRef](#)]
6. Herrmann, A.; Greuner, H.; Fuchs, J.C.; de Marné, P.; Neu, R.; ASDEX Upgrade Team. Experiences with tungsten coatings in high heat flux tests and under plasma load in ASDEX Upgrade. *Phys. Scr.* **2009**, *T138*, 014059. [[CrossRef](#)]
7. Cui, S.; Simmonds, M.; Qin, W.; Ren, F.; Tynan, G.R.; Doerner, R.P.; Chen, R. Thermal conductivity reduction of tungsten plasma facing material due to helium plasma irradiation in PISCES using the improved 3-omega method. *J. Nucl. Mater.* **2017**, *486*, 267–273. [[CrossRef](#)]
8. Kajita, S.; De Temmerman, G.; Morgan, T.; Van Eden, S.; de Kruif, T.; Ohno, N. Thermal response of nanostructured tungsten. *Nucl. Fusion* **2014**, *54*, 033005. [[CrossRef](#)]
9. Uytendhouwen, I.; Massaut, V.; Linke, J.; Van Oost, G. Plasma wall interaction phenomena on tungsten armour materials for fusion applications. In Proceedings of the International Youth Nuclear Congress 2008, Interlaken, Switzerland, 20–26 September 2008.
10. Lemahieu, N.; Linke, J.; Pintsuk, G.; Van Oost, G.; Wirtz, M.; Zhou, Z. Performance of yttrium doped tungsten under “edge localized mode”-like loading conditions. *Phys. Scr.* **2014**, *T159*, 014035. [[CrossRef](#)]
11. Shirokova, V.; Laas, T.; Ainsaar, A.; Priimets, J.; Ugaste, U.; Väli, B.; Gribkov, V.A.; Maslyaev, S.A.; Demina, E.V.; Dubrovsky, A.D.; et al. Armor materials’ behavior under repetitive dense plasma shots. *Phys. Scr.* **2014**, *T161*, 014045. [[CrossRef](#)]
12. De Temmerman, G.C.; Bystrov, K.E.; Zielinski, J.J.; Balden, M.; Matern, G.; Arnas, C.; Marot, L. Nanostructuring of molybdenum and tungsten surfaces by low-energy helium ions. *J. Vac. Sci. Technol. A Vac. Surf. Film.* **2012**, *30*, 41306. [[CrossRef](#)]
13. Tripathi, J.K.; Novakowski, T.J.; Hassanein, A. Tailoring molybdenum nanostructure evolution by low energy He⁺ ion irradiation. *Appl. Surf. Sci.* **2015**, *353*, 1070–1081. [[CrossRef](#)]
14. Sinclair, G.; Tripathi, J.K.; Diwakar, P.K.; Hassanein, A. Structural response of transient heat loading on molybdenum surface exposed to low-energy helium ion irradiation. *Nucl. Fusion* **2016**, *56*, 36005. [[CrossRef](#)]
15. Brooks, J.N.; El-Guebaly, L.; Hassanein, A.; Sizyuk, T. Plasma-facing material alternatives to tungsten. *Nucl. Fusion* **2015**, *55*, 43002. [[CrossRef](#)]
16. Sinclair, G.; Tripathi, J.K.; Diwakar, P.K.; Hassanein, A. Melt layer erosion during ELM-like heat loading on molybdenum as an alternative plasma-facing material. *Sci. Rep.* **2017**, *7*, 12273. [[CrossRef](#)]
17. Rieth, M.; Dudarev, S.L.; De Vicente, S.M.G.; Aktaa, J.; Ahlgren, T.; Antusch, S.; Armstrong, D.E.J.; Balden, M.; Baluc, N.; Barthe, M.-F.; et al. Recent progress in research on tungsten materials for nuclear fusion applications in Europe. *J. Nucl. Mater.* **2013**, *432*, 482–500. [[CrossRef](#)]
18. Cottrell, G.A. Sigma phase formation in irradiated tungsten, tantalum and molybdenum in a fusion power plant. *J. Nucl. Mater.* **2004**, *334*, 166–168. [[CrossRef](#)]
19. Sizyuk, T.; Hassanein, A. Dynamic analysis and evolution of mixed materials bombarded with multiple ions beams. *J. Nucl. Mater.* **2010**, *404*, 60. [[CrossRef](#)]

20. Sharpe, J.P.; Kolasinski, R.D.; Shimada, M.; Calderoni, P.; Causey, R.A. Retention behavior in tungsten and molybdenum exposed to high fluences of deuterium ions in TPE. *J. Nucl. Mater.* **2009**, *390*, 709–712. [[CrossRef](#)]
21. Richetta, M.; Gaudio, P.; Montanari, R.; Pakhomova, E.; Antonelli, L. Laser pulse simulation of high energy transient thermal loads on bulk and plasma sprayed W for NFR. *Mater. Sci. Forum* **2017**, *879*, 1576–1581. [[CrossRef](#)]
22. Montanari, R.; Pakhomova, E.; Pizzoferrato, R.; Richetta, M.; Varone, A. Laser pulse effects on plasma sprayed and bulk tungsten. *Metals* **2017**, *7*, 454. [[CrossRef](#)]
23. Gaudio, P.; Montanari, R.; Pakhomova, E.; Richetta, M.; Varone, A. W-1%La₂O₃ submitted to a single laser pulse: Effect of particles on heat transfer and surface morphology. *Metals* **2018**, *8*, 389. [[CrossRef](#)]
24. Rubel, M.; Brezinsek, S.; Coenen, J.W.; Huber, A.; Kirschner, A.; Kreter, A.; Petersson, P.; Philipps, V.; Pospieszczyk, A.; Schweer, B.; et al. Overview of wall probes for erosion and deposition studies in the TEXTOR tokamak. *Matter Radiat. Extrem.* **2017**, *2*, 87–104. [[CrossRef](#)]
25. *International Centre for Diffraction Data*; JCPDS: Newtown Square, PA, USA, 1907.
26. Williamson, G.K.; Smallman, R.A. Dislocation densities in some annealed and cold-worked metals from measurements on the X-ray Debye-Scherrer spectrum. *Philos. Mag.* **1956**, *1*, 34–45. [[CrossRef](#)]
27. Gondi, P.; Donato, A.; Montanari, R.; Sili, A. Miniaturized test method for the mechanical characterization of structural materials for fusion reactors. *J. Nucl. Mater.* **1996**, *233*, 1557–1560. [[CrossRef](#)]
28. Francucci, M.; Gaudio, P.; Martellucci, S.; Richetta, M. Spectroscopy methods and applications of the Tor Vergata laser-plasma facility driven by GW-level laser system. *Int. J. Spectrosc.* **2011**, *2011*. [[CrossRef](#)]
29. Dong, H.; Wen, B.; Melnik, R. Relative importance of grain boundaries and size effects in thermal conductivity of nanocrystalline materials. *Nat. Sci. Rep.* **2014**, *4*, 7037. [[CrossRef](#)]
30. Swartz, E.T.; Pohl, R.O. Thermal boundary resistance. *Rev. Mod. Phys.* **1989**, *61*, 605. [[CrossRef](#)]
31. Nan, C.-W.; Birringer, R.; Clarke, D.R.; Gleiter, H. Effective thermal conductivity of particulate composites with interfacial thermal resistance. *J. Appl. Phys.* **1997**, *81*, 6692–6699. [[CrossRef](#)]
32. Yang, H.-S.; Bai, G.-R.; Thompson, L.; Eastman, J. Interfacial thermal resistance in nanocrystalline yttria-stabilized zirconia. *Acta Mater.* **2002**, *50*, 2309–2317. [[CrossRef](#)]
33. Paradis, P.F.; Ishikawa, T.; Koike, N. Non-contact measurements of the surface tension and viscosity of molybdenum using an electrostatic levitation furnace. *Int. J. Refract. Met. Hard Mater.* **2007**, *25*, 95–100. [[CrossRef](#)]
34. Paradis, P.F.; Ishikawa, T.; Fujii, R.; Yoda, S. Physical properties of liquid and undercooled tungsten by levitation techniques. *Appl. Phys. Lett.* **2005**, *86*, 041901. [[CrossRef](#)]
35. Cagran, C.; Wilthan, B.; Pottlacher, G. Normal spectral emissivity at a wavelength of 684.5 nm and thermophysical properties of solid and liquid molybdenum. In Proceedings of the 5th Symposium on Thermophysical Properties, Boulder, CO, USA, 23–28 June 2003.
36. Ishikawa, T.; Paradis, P.-F.; Okada, J.T.; Kumar, M.V.; Watanabe, Y. Viscosity of molten Mo, Ta, Os, Re, and W measured by electrostatic levitation. *J. Chem. Thermodyn.* **2013**, *65*, 1–6. [[CrossRef](#)]
37. Straus, J.; Kolacek, K.; Schmidt, J.; Frolov, O.; Vilemova, M.; Matejicek, J.; Jager, A.; Juha, L.; Toufarova, M.; Choukourov, A.; et al. Response of fusion plasma-facing materials to nanosecond pulses of extreme ultraviolet radiation. *Laser Part. Beam* **2018**, *36*, 293–307. [[CrossRef](#)]
38. Eksaeva, A.; Borodin, D.; Romazanov, J.; Kirschner, A.; Kreter, A.; Eichler, M.; Rasinski, M.; Pospieszczyk, A.; Unterberg, B.; Brezinsek, S.; et al. Surface roughness effect on Mo physical sputtering and re-deposition in the linear plasma device PSI-2 predicted by ERO2.0. *Nucl. Mater. Energy* **2019**, *19*, 13–18. [[CrossRef](#)]
39. Wurster, S.; Baluc, N.; Battabyal, M.; Crosby, T.; Du, J.; Garca-Rosales, C.; Hasegawa, A.; Hoffmann, A.; Kimura, A.; Kurishita, H.; et al. Recent progress in R&D on tungsten alloys for divertor structural and plasma facing materials. *J. Nucl. Mater.* **2013**, *442*, S181–S189.
40. Linsmeier, C.; Rieth, M.; Aktaa, J.; Chikada, T.; Hoffmann, A.; Hoffmann, J.; Houben, A.; Kurishita, H.; Jin, X.; Li, M.; et al. Development of advanced high heat flux and plasma-facing materials. *Nucl. Fusion* **2017**, *57*, 092007. [[CrossRef](#)]

